JGR Atmospheres

RESEARCH ARTICLE
10.1029/2019JD031329

Determination of Global Mean Eddy Diffusive Transport in the Mesosphere and Lower Thermosphere From Atomic Oxygen and Carbon Dioxide Climatologies

G. R. Swenson[1], C. C. J. H. Salinas[2,3,4], F. Vargas[1], Y. Zhu[5], M. Kaufmann[5,6], M. Jones Jr.[7], D. P. Drob[7], A. Liu[8], J. Yue[9], and J. H. Yee[10]

[1]Electrical and Computer Engineering, University of Illinois, Urbana, IL, USA, [2]Taiwan International Graduate Program-Earth Systems Science, Academia Sinica, Taipei, Taiwan, [3]Department of Atmospheric Sciences, National Central University, Taoyuan City, Taiwan, [4]Center for Astronautical Physics and Engineering, National Central University, Taoyuan City, Taiwan, [5]Institute of Energy and Climate Research (IEK-7), Forschungzentrum Juelich GmbH, Juelich, Germany, [6]Physics Department, University of Wuppertal, Wuppertal, Germany, [7]Space Science Division, Naval Research Laboratory, Washington, DC, USA, [8]Physical Science, Embry-Riddle Aeronautical University, Daytona Beach, FL, USA, [9]Heliophysics Division, NASA Goddard Space Flight Center, Greenbelt, MD, USA and Catholic University of America, DC, USA, [10]Applied Physics Laboratory, The Johns Hopkins University, Baltimore, MD, USA

Key Points:
- Global mean vertical transport velocities of atomic oxygen in the MLT (80–105 km) were determined from SABER and SCIAMACHY
- The resolution of historical differences in the eddy diffusion coefficients between O and CO_2 have been resolved (above 85 km)
- The values of eddy diffusion coefficients increase above 85 km to a maximum above 100 km, where little information has been available

Correspondence to:
G. R. Swenson,
swenson1@illinois.edu

Citation:
Swenson, G. R., Salinas, C. C. J. H., Vargas, F., Zhu, Y., Kaufmann, M., Jones, M., et al. (2019). Determination of global mean eddy diffusive transport in the mesosphere and lower thermosphere from atomic oxygen and carbon dioxide climatologies. *Journal of Geophysical Research: Atmospheres*, *124*, 13,519–13,533. https://doi.org/10.1029/2019JD031329

Received 9 JUL 2019
Accepted 1 OCT 2019
Accepted article online 29 OCT 2019
Published online 5 DEC 2019

Author Contributions
Conceptualization: G. R. Swenson
Methodology: G. R. Swenson
Software: G. R. Swenson
Validation: G. R. Swenson
Writing - Original Draft: G. R. Swenson
Formal Analysis: G. R. Swenson
Project Administration: G. R. Swenson
Writing - review & editing: G. R. Swenson

Abstract Quantifying the eddy diffusion coefficient profile in the mesosphere and lower thermosphere (MLT) is critical to the constituent density distributions in the upper mesosphere and thermosphere. Previous work by Swenson et al. (2018, https://doi.org/10.1016/j.jastp.2018.05.014) estimated the global mean eddy diffusion (k_{zz}) values in the upper mesosphere using atomic oxygen (O), derived from Sounding of the Atmosphere using Broadband Emission Radiometry (SABER) hydroxyl (OH). In this study, vertical eddy diffusive transport velocities of O were determined from continuity of mass in the mesopause region (80–97 km), primarily via the HO_x chemistry. Global average constituent climatology from previously deduced SABER ozone (O_3) and atomic hydrogen (H) was applied. Furthermore, we extended the global mean eddy transport velocities to new heights (105 km) in the MLT using the newly available global mean Scanning Imaging Absorption Spectrometer for Atmospheric Chartography (SCIAMACHY) data. The combined method of determining O_3 loss and O density climatology from SCIAMACHY, as well as an improved global mean background atmosphere from SABER, provides new information for eddy diffusion determination in the MLT. Three prominent results to emerge from this study include (i) global mean k_{zz} profiles between 80 and 105 km derived from MLT constituent climatologies, SABER, and SCIAMACHY global mean O density profiles averaged for approximately one solar cycle, (ii) determination of O eddy diffusion velocities in the MLT consistent between two satellite measurements and the thermosphere-ionosphere-mesosphere-electrodynamics general circulation model, and (iii) resolution of historically large differences between deduced k_{zz} determined from O versus CO_2 by analysis of SABER and SCIAMACHY measurements.

1. Introduction

1.1. Eddy Diffusion in the MLT: Background and Relevance

Oxygen compounds (specifically, atomic, diatomic, and triatomic oxygen, or O, O_2, and O_3) are fundamental to the aeronomy of the middle and upper atmosphere. The distribution of these compounds (mainly O and O_2) in the upper mesosphere and thermosphere is determined by dynamical, chemical, photochemical, and diffusive processes in the mesopause region (80–105 km). Specifically, the upper mesosphere and lower thermosphere (MLT) are important regions where the background atmosphere transitions are from being well-mixed, controlled by small-scale wave dissipation and turbulence (approximated in most general circulation models as eddy diffusion, k_{zz}), to diffusively separated. The concept of k_{zz} was pioneered >50 years ago by Colegrove et al. (1965, 1966) to characterize the turbulent-induced diffusion and continues to be a prominent area of research in the MLT (e.g., Fritts & Alexander, 2003, 2012), and ionosphere-thermosphere (IT; e.g., Pilinski & Crowley, 2015; Qian et al. 2009, 2013; Salinas et al., 2016) communities.

The waves from the lower atmosphere (tidal and gravity), propagating upward from below, are filtered en route by the background atmosphere and planetary waves and are largely responsible for generating

turbulent mixing that affects the MLT dynamics and drives k_{zz}. Numerous studies (e.g., Fukao et al., 1994; Gardner, 2018; Kirchhoff & Clemesha, 1983; Khattatov et al., 1996; Lübken, 1997; Liu, 2009; Rao et al., 2001; Sasi & Vijayan, 2001) have investigated turbulence and gravity wave effects and estimated local k_{zz} in the MLT. As an example, a high-resolution mechanistic global circulation model (GCM) was coupled with a chemistry-transport model using wave sources from below to drive the MLT minor constituent distributions Grygalashvyly et al., 2011, 2012. They used an advanced parameterization of turbulent diffusion described by Becker and von Savigny (2010). The atmosphere above is also coupled to k_{zz} in the MLT. Recent modeling studies using GCMs (e.g., Jones et al., 2017; Liu et al., 2018; Pilinski & Crowley, 2015; Qian et al., 2009; 2013) have demonstrated just how sensitive thermospheric and ionospheric mass and plasma densities in general circulation models can be to underlying k_{zz} and, more specifically, to global mean k_{zz}. The major focus of this study, simply put, is to establish the global mean k_{zz} in the MLT region from the global mean O and CO_2 climatology of the MLT. The climatological global mean k_{zz} profile can provide diffusion information to models which are working to couple the regions below and above, while more precisely describing the diffusive transport and composition in the MLT region and above.

In addition to oxygen in the MLT, the population distribution and flux of metals are strongly dependent on k_{zz}. Resonant lidar systems have measured the climatology of metal distributions with altitude and Doppler lidars have measured constituent fluxes. There is very large uncertainty (a few to 300 tons/day) in the global cosmic dust input of metal to the MLT (Plane et al., 2015). Part of the uncertainty arises from the uncertainty of metal loss processes from the MLT to the lower atmosphere. Gardner and Liu (2014) and Gardner and Huang (2016) estimated the global cosmic dust input based on sodium (Na) lidar measurements. Liu and Gardner (2005), Gardner and Liu (2010), and Gardner, Liu, et al. (2014) have estimated such transport processes due to gravity wave dissipation and turbulence using a ground-based Na lidar. Simultaneous rocket in situ and lidar measurements have also measured overturning scales contributing to vertical transport (Larsen et al. 2004, Liu et al., 2004). This diffusive vertical transport plays a major role in determining the mean density profiles of metal atoms. The source of these metals (from ablation of interplanetary dust particles entering the atmosphere) must be balanced by the downward transport processes and chemical sources and sinks. Analogous to atomic oxygen loss described by Swenson et al. (2018) (S18), mass conservation of metals requires the input rate to be balanced by their loss to the lower atmosphere, below 80 km. A better knowledge of k_{zz} enables better estimation of the metal loss that leads to a better estimation of the source input rate from meteors. The global average k_{zz} is a key to providing improved knowledge of metal transport processes in the MLT. The MLT is the source region for the neutral and ion populations in the thermosphere. Early studies of thermospheric profiles of Mg^+ (Gerard & Monfils, 1978) led to morphological observational studies of the ion (Fesen & Hays, 1982) and fountain transport at low latitudes in the *E* region (Mende et al., 1985). Gardner et al. (1999) observed and quantified latitudinal neutral Na and Fe densities as well as ions well into the upper thermosphere with the GLO-1 spectrometer instrumentation on Space Shuttle missions. Measurement technology development in lidar has led to the ability to sense Na to above 170 km and to use Doppler methods to measure temperature and winds to 140 km (Liu et al., 2016).

Accurately simulating the mass density, neutral composition, and electron density of the IT system, and its variability, depends heavily on understanding processes in the MLT region. For example, a recent issue involving global-mean eddy diffusion (k_{zz}) centers on its role in driving the thermosphere-ionosphere annual oscillation (AO; winter solstice maximum and summer solstice minimum) and semiannual oscillations (SAO; equinoctal maximum and solstice minimum). Knowledge of global mean thermospheric density is crucial for the satellite drag force and satellite lifetime predictions, especially for LEO (Low Earth Orbit) satellites. The theories describing the SAO and AO continue to evolve with recent interest. It is well known that solar forcing and geomagnetic forcing are not enough to drive the global mean AO and SAO in thermospheric density (Field et al., 1998; Jacchia, 1964, 1970, 1971; Lal, 1998; 1992; Paetzold & Zschörner, 1961; Prolss, 1995; Walterscheid, 1982). Instead, the "thermospheric spoon" mechanism caused by the seasonally varying thermosphere general circulation was proposed as the primary driver of the SAO (Fuller-Rowell, 1998). In order to account for the discrepancy between models and observations with the "thermospheric spoon" effect, Qian et al. (2009) suggested that global-mean eddy k_{zz} may also be important in generating the AO and SAO in the IT region. They varied k_{zz} at the lower boundary of the thermosphere-ionosphere electrodynamics-GCM based on satellite neutral density measurements in the upper thermosphere to differentially affect the O density and molecular species densities to reproduce thermospheric AO and SAO

variations. Although Jones et al. (2018) demonstrated that seasonally varying k_{zz} was sufficient, but not necessary, to drive a thermospheric general circulation model to self-consistently reproduce the climatological IT SAO, they did conclude that seasonally varying tidal mixing and k_{zz} played a notable role in modulating the amplitude of the IT SAO.

Even lighter species (H and He) that do not become major species in the Earth's atmosphere until the upper thermosphere (altitudes > ~600 km) are affected by k_{zz} in the MLT. For example, escape fluxes of H have been studied using the upper limit of molecular diffusion supporting the escape flux at the base of the exosphere (e.g., Catling & Zahnle, 2009; Catling & Kasting, 2017), with aeronomic considerations of H composition from the stratosphere to the base of the exosphere, and Jeans escape. Early studies including Colegrove et al. (1966) describe the importance and early calculations of vertical H transport at the turbopause (~100 km), followed by detailed studies by Liu and Donahue (1974), Hunten (1973), and Hunten and Strobel (1974). The upper limit of loss at the exobase is constrained by the upper limit of molecular diffusion, which is temperature dependent. This was adopted as the limit because little was known about other potential limits, such as the eddy diffusion rates at the mesopause. Simply put, global average k_{zz} values determined herein, as well as refinements in the knowledge of composition including H, H_2, CH_4, and H_2O at the turbopause, form a basis to revisit fluxes at the MLT. A substantial change in limiting flux due to lower k_{zz} will also affect escape rates of H in the exosphere (Jeans, 2009; Shizgal & Arkos, 1996).

1.2. Introducing the Method

Deducing k_{zz} from ground-based and rocket observations (e. g. Gardner, 2018; Lübken, 1997) has a rich history in the MLT community. Since space-borne techniques prohibit direct measurements of eddy/turbulence scales, using satellite measured tracers can be used to derive the global k_{zz}. Recently, long-term satellite measurements of neutral constituents in the MLT have emerged and been analyzed (e.g., Salinas et al., 2016; Swenson et al., 2018) such that global mean k_{zz} can now be deduced. In this case, the term *global* means from averaging ~ 1 solar cycle of constituents from data at middle and low latitudes from both hemispheres. Salinas et al. (2016) used global SABER (Sounding of the Atmosphere using Broadband Emission Radiometry) CO_2 observations to derive global-mean k_{zz} profiles that span more than one solar cycle. It was then shown that the seasonality of these coefficients was consistent with global-mean k_{zz} from gravity wave parameterizations (Garcia et al., 2014; Jones et al., 2017). Salinas et al. (2016) then forced the thermosphere-ionosphere electrodynamics-GCM lower boundary with their CO_2-derived global-mean k_{zz} and found that they could not reproduce the results of Qian et al. (2009) (i.e., k_{zz} could not drive the observed AO and SAO in the I/T region). Similar to Jones et al. (2018), they concluded that the IT SAO (and therefore IT constituents) was sensitive to changes in global-mean k_{zz}, but not a dominant driver of the SAO. These studies demonstrate that an accurate global-mean k_{zz} is important in understanding the thermospheric and ionospheric neutral and plasma densities and their variations.

Historically, k_{zz} has been determined from the meteorology from below (e.g., Grygalashvyly et al., 2011) or it has been calculated in order to define variability of O in the thermosphere (e.g., Qian et al., 2009). The focus of this study is to determine the global mean k_{zz} profile from the climatology of O density measurements in mesosphere, similar to S18. The vertical distributions of all constituents in the MLT are uniquely defined by the eddy and molecular diffusion coefficient profiles through the relative dominance of one versus the other. Thermospheric O density is primarily defined in altitude by its mass (molecular diffusion) but in the mesosphere below 105 km by the chemical loss and eddy diffusion. The downward flux of O and chemistry governs the O loss rate which must be balanced by its production rate (via photodissociation) ~120 km. It is the knowledge of constituent climatologies and loss chemistry that enables this study to determine improved MLT k_{zz} profiles.

An alternative to the use of direct wind or temperature observations in estimating eddy diffusion would be the use of chemical constituent observations. Early studies conducted by Allen et al. (1981) and others used rocket observations to derive local eddy diffusion coefficients from different chemical constituents. Advances in our observational capacity have now allowed us to measure chemical species on a global scale. Ideally, tracers with a photochemical lifetime significantly larger than its transport lifetime should be used to derive k_{zz} so that the complicating factors of chemical production and loss can be largely ignored. CO_2 is an example of this (Garcia et al., 2014; Lopez-Puertas et al., 2000; Smith et al., 2011). Actually, even for studies interested in looking at the variability of CO_2 in time scales greater than 1,000 days, CO_2's photochemistry is fairly well understood (Garcia et al., 2014). Thus, most of its uncertainties are in the transport processes.

Consequently, when taking its global-mean, uncertainties in its vertical profile can solely be attributed to uncertainties in k_{zz}. Salinas et al. (2016) took exactly this approach by utilizing SABER CO_2 observations to derive global-mean k_{zz} throughout the MLT region. The present study, in contrast, takes on the challenge of deriving k_{zz} from chemically active species and follows the recent work of S18, where 12 years of SABER O were used to determine a global mean of k_{zz}.

An important aspect of this study is the determination of k_{zz} associated with the downward flux of atomic oxygen driven by chemical loss. The flux is due to turbulence, dissipating gravity and large-scale waves, and molecular diffusion which contribute to the transport of O with respect to the background atmosphere. The effective diffusivity described by Grygalashvyly et al. (2012) is a paramaterization that has assumptions similar to that used in this 1-D study. Turbulence as well as mixing processes associated with dissipating gravity waves contribute to the eddy diffusion processes. Guo et al. (2017) provides a summary of the history of the evolution of turbulence measurements and estimated the turbulence transport of heat in the MLT that can resolve both gravity waves and turbulence spectra. Gardner (2018) analyzed statistical measurements by Na lidars to determine the vertical transport of O at two mountain stations. These studies clearly demonstrate that both dissipating gravity waves and turbulence share the role of the vertical eddy transport of O in the MLT.

1.3. What is New and Unique in This Study Compared to S18?

S18 presented an analysis of the global average of SABER O from OH valid between 80 and 96 km. The method, unique to atomic oxygen, recognizes O is produced in the 120–130 km altitude region and is chemically lost below 100 km. Well-known loss chemistry and rates were used to determine the diffusive flux of O. A key discovery was the MLT column density, previously considered to be constant, varies with the solar cycle. The background atmosphere used to define the recombination chemistry, dominated by O_3 production, employed the NRLMSISE-00 model atmosphere. An altitude profile of k_{zz} was calculated from the downward flux of O due to eddy processes, with value of 5–8 $\times$ 10^5 cm^2/s, and was compared to other recent k_{zz} determinations. The standard deviation of the annual averaged global mean k_{zz} was $< 5\%$.

A number of additions and significant improvements were made since the earlier S18 study including the following:

(i) The climatological values of O_3 and H chemistry producing O_3 loss best represents the climatology of the main atmospheric constituents involved in O loss;
(ii) An additional O data base from the SCIAMACHY (Scanning Imaging Absorption Spectrometer for Atmospheric Chartography) instruments on Envisat from both OH (valid 80–96 km) and O(^{1}S) (valid 90–105 km); significant improvements include the following:
    (a) changing the "background atmosphere" to the SABER climatology global mean state,
    (b) providing relevance and insights of global mean k_{zz},
    (c) including the temperature gradient term (relatively minor) in the expression for the determination of k_{zz},
    (d) addressing O density sensitivity to the chemistry and diffusion transport times in response to k_{zz}.

2. Description of Method and Analysis

2.1. Global Mean [O], [O_3], [H], and Total (SABER) N_2 and O_2 Densities

Atomic oxygen density profile ([O]) global measurements in the upper mesosphere and lower thermosphere have been made by a number of spacecraft sensors in recent years. Some of these measurements provide climatologies over a solar cycle, the period of influence of [O] variation through dissociative processes in the upper atmosphere.

Limb measurements using OH emission from SABER instrument (described by Russell et al. 1999) for 11 years (2002–2013) (Mlynczak et al., 2013) were refined by Mlynczak et al. (2018) and extended to 16 years for ±55°. SABER is aboard the TIMED (Thermosphere, Ionosphere, Mesosphere Energetics and Dynamics) satellite which was launched on 7 December 2001. The mission has a latitudinal coverage of 82°N to 53°S or 53°N to 82°S with alternating coverage due to the spacecraft yaw cycle every 60 days. The mission has an orbital period of 1.6 hr and a local time precession of 12 min per day. These SABER OH observations processed for O densities formed the basis for the analysis described in S18. The altitude of maximum volume emission rate is ~87 km, which provides a reasonable signal-to-noise ratio for limb viewing the layer to invert [O] between 80 and 96 km in altitude.

A new data set included in the current version of our model comes from the SCIAMACHY instrument on Envisat, which measured a near global O (i.e., spanning 50°S to 80°N) from O(^{1}S) green line emissions (Kaufmann et al., 2014). The altitude of maximum volume emission rate for O(^{1}S) is ~96 km, providing a reasonable signal-to-noise ratio of O density between 90 and 105 km and allowing us to extend our chemical O model (and thus our k_{zz} values) to 105 km. Note that the [O] measured from SCIAMACHY O(^{1}S) (Kaufmann et al., 2014) has been independently validated against Optical Spectrograph and Infrared Imaging System [O] data from O_2 A-band measurements onboard the Odin satellite (Sheese et al., 2011) at low latitudes between 2007 and 2009. More recently, Zhu and Kaufmann (2018) have also deduced O densities from SCIAMACHY OH measurements in the 80–96 km region and found some significant differences between those derived from SABER OH radiance measurements and those derived from SCIAMACHY OH nightglow measurements. The altitude range of O densities derived from SCIAMACHY O(^{1}S) and SCIAMACHY OH data overlaps between 90 and 96, with minimal difference (<15-20%) between them. In our study, we employ O densities from both SCIAMACHY OH and SABER OH, as well as SCIAMACHY O(^{1}S).

Another data set used in the present investigation that extends from the work of S18 is the global mean of [O_3] from Smith et al. (2013) derived from nine different instruments, including SABER. The [O_3] climatology from Smith et al. (2013) covers the period between 1991 and 2012. Global means from four satellites including SABER 9.6 and 1.27 μm channels all compared favorably. The nighttime SABER measurements between 80 and 100 km in Figure 12 of Smith et al. (2013) were used in this analysis. Mlynczak et al. (2018) suggests that the Smith et al. (2013) daytime SABER [O_3] may be too large but there is high confidence in the nighttime measurements. We also make use of the global mean [H] climatologies initially determined by Mlynczak et al. (2014) and revised by Mlynczak et al. (2018). The [H] determination was refined with the consideration of refined SABER [O] (see Mlynczak et al., 2018). [O_3] and [H] global mean climatologies are key elements that provide a major improvements in the loss chemistry of O.

The global mean background atmosphere was measured by SABER (Mlynczak et al., 2014). Mlynczak et al. (2014) deduced the global [H] climatology by assuming the ozone loss chemistry ($O_3 + H = OH + O_2$) equals production ($O + O_2 + M$), where SABER O, O_2, and M and Smith et al. (2013) O_3 densities were used to solve for the unknown [H], and the background atmosphere was that measured by SABER. We reversed the calculation herein, using Mlynczak et al. (2018) H, and deduced the SABER equivalent N_2 and O_2. Note that the SABER N_2 and O_2 used are $\sim$ 20% lower between 80 and 90 km than the NRLMSISE-00 model values used in S18. In summary, all of the data employed in the computation of the global mean k_{zz} are "climatological" data, with the assumption made by Mlynczak et al. (2018) in the determination of [H].

2.2. Overview of the [O] Method

Since this study represents a major revision of our original work, we describe in detail the methodology employed to derive k_{zz} values. The method involves calculating the net downward diffusion flux of O, given the condition O is produced in the lower thermosphere from photodissociation of O_2 near 120 km, where it diffuses throughout the thermosphere. The production below 105 km is assumed to be negligible [see section 4]. In the mesopause region (80–105 km), the eddy flux for O is downward, and the molecular diffusion flux of O is upward, with the dominant downward eddy flux transported O being lost via chemical processes. The downward O flux must balance, on the average, the chemical loss of odd oxygen, which is determined from well-established chemistry.

The differential flux, or flux divergence with versus altitude is defined as (see equation (9) of Colegrove et al., 1966, and equation (1) of Salinas et al., 2016):

$$\frac{d\phi_O}{dz} = P - L \tag{1}$$

where $\phi_O = v_O[O]$ (v_O is the diffusion velocity). In the case of atomic oxygen below 105 km,

$$\frac{d\phi_O}{dz} = -L \tag{2}$$

Equation (9) of Colegrove et al. (1966) has both the production (P) and loss (L) terms, but S18 reduced this to L only below 105 km, the altitude region over which the k_{zz} is being determined herein. A criterion in the solution of the divergence that was not included in the earlier studies (Allen et al., 1981; Colegrove

et al., 1966) is the fact that the downward flux of atomic oxygen, at and below 105 km, must supply the total chemical loss, or integral loss, that is,

$$\phi_O(z) = \int_{z=80}^{z} (-L)\, dz' \tag{3}$$

The chemical losses are in the dark period where O_3 is chemically lost rather than being photodissociated in daytime. The daily average loss of O is assumed one-half the nighttime loss, the same assumption used in S18. In this study, we are only concerned with the chemical loss of odd oxygen. In addition to O_3 chemistry, we also consider O losses through three-body recombination, two-body collisions with O_3, and HO_2 chemistry, where the densities used to calculate the chemical rates were calculated using the global mean atmosphere defined above. This model is consistent with Smith et al. (2010) and Mlynczak et al. (2013) chemical loss processes of odd oxygen.

The main O loss in the mesosphere is due to the net loss of odd oxygen due to O_x catalysis by HO_x described by

$$O + O_2 + M \rightarrow O_3 + M, \quad k_1 = 6.4 \times 10^{-34}(300/T)^{2.4} \tag{4}$$

and subsequently,

$$O_3 + H \rightarrow OH^* + O_2, \quad k_2 = 1.4 \times 10^{-10} \exp(-470/T) \tag{5}$$

followed by

$$O + OH \rightarrow O_2 + H, \quad k_3 = 2.2 \times 10^{-11} \exp(120/T) \tag{6}$$

where the rate coefficients k_1, k_2, and k_3 are given by Sander et al. (2011) and OH in equation (6) includes OH and $OH^*(v \leq 6)$. Regarding the HO_x chemistry above, since the O_3 produced in equation (4) is all destroyed in equation (5), the loss rate can be computed using either chemical process in determination of the odd-oxygen loss rate from the HO_x reactions.

Under the assumption of chemical equilibrium, one O is lost when one O_3 is produced (equation (4)), followed by OH formation (equation (5)), and subsequent OH destruction by O (equation (6)) where the second O is lost. The S18 study used equation (4), but in doing so, relied on model values for some of the parameters, including $[N_2]$ and $O[_2]$. In this study, the loss is determined from equation (5). The rationale for this consideration is that the mean $[O_3]$ and [H] climatologies deduced from SABER best represent the global mean state for ozone chemistry in the MLT and are consistent with the SABER [O] values herein.

The downward flux of O below a given altitude is expressed in equation (7) below, where the loss terms include that due to ozone (i.e., term 1 in equation (7)),

$$\phi_O(z) = \int_{z=80}^{z} (-2k_2[O_3][H] - 2k_4[O]^2[M] - 2k_5[O][O_3] - 2k_6[H][O_2][M])\, dz' \tag{7}$$

where the first term is the loss due to the HO_x process, where the Integer 2 quantifies the number of O atoms lost in the process. The minor contributions from other chemical reactions are the Terms 2–4 in equation (7), where the processes are described in S18 and the rate coefficients (k_4, k_5, and k_6) in Sander et al. (2011). The second term is from three-body recombination (O + O + M), the third from $O + O_3$, and the forth from HO_2. S18 included the metal chemistry also, but found it to be insignificant, and consequently it is not included here. Calculations for equation (7) are determined for each kilometer, between 80 and 105 km, and the downward flux is determined from the integral loss below each altitude. The losses above 100 km are dominated by three-body recombination (the second term in the integral expression). We assume zero loss below 80 km.

Once the vertical flux is calculated from equation (7), the downward diffusion velocity is equation (8):

$$v_O(z) = \frac{\phi_O(z)}{[O](z)} \tag{8}$$

Calculations are made for each altitude between 105 and 80 km, for the flux (equation (7)), and total O transport velocity (equation (8)). Note that this is the total downward velocity, that is, the combined eddy and molecular components.

Note that the vertical flux of any species at MLT altitudes is the aggregate of the dynamical processes including gravity waves and atmospheric tides, (e.g., Jones et al., 2014) and chemical fluxes (e.g., Gardner & Liu, 2010), the flux due to both eddy and molecular diffusion, and advection. There is no attempt in this study to partition the components contributing to the total, as was done by Jones et al. (2017) and also by Gardner (2018). However, since Jones et al. (2017) demonstrated that the vertical transport due to eddy diffusion was the dominant process acting to transport O vertically between ~75 and 105 km, we assume the *effective* eddy diffusion velocity of O can be computed by subtracting the molecular diffusion velocity of O ($v_{O,md}(z)$), relative to the background atmosphere, from the total O velocity. This is especially important for the transition region between 95 and 105 km.

The total diffusive flux is described in equation (9). S18 found the temperature term to be relatively small, but it is included here. The eddy diffusion velocity is calculated in equation (11) where the molecular diffusion component is defined in equation (10) and is subtracted from the total in equation (11).

$$\phi_O(z) = -D_i[O]\left(\frac{1}{H_i} + \frac{1}{T}\frac{dT}{dz} + \frac{1}{[O]}\frac{d[O]}{dz}\right) - k_{zz}[O]\left(\frac{1}{H} + \frac{1}{T}\frac{dT}{dz} + \frac{1}{[O]}\frac{d[O]}{dz}\right) \tag{9}$$

where the general expression for the molecular diffusion velocity for a given species i is

$$v_{n_i,md}(z) = -D_i\left(\frac{1}{H_i} + \frac{1}{T}\frac{dT}{dz} + \frac{1}{[n_i]}\frac{d[n_i]}{dz}\right) \tag{10}$$

$$v_{O,eddy}(z) = v_O(z) - v_{O,md}(z) \tag{11}$$

The effective k_{zz} defined in equation (12) is calculated from the eddy diffusion velocity defined in equation (11).

$$k_{zz} = -\frac{v_{O,eddy}}{\left(\frac{1}{H} + \frac{1}{T}\frac{dT}{dz} + \frac{1}{[O]}\frac{d[O]}{dz}\right)} \tag{12}$$

The terms for the above are defined as

- D_{ij}: mutual diffusion coefficient for ith and jth gases ($D_{O,N_2} = 0.26(T/T_0)^{1.76}(P_0/P)$)
- D_i: species molecular diffusion coefficient ($1/D_i = \sum_{j\neq i} n_j/ND_{ij}$)
- g: acceleration of gravity
- H: scale height ($\kappa T/mg$)
- H_i: species scale height ($\kappa T/m_i g$)
- k_{zz}: eddy diffusion coefficient
- κ: Boltzmann constant
- m_i: species molecular weight
- m: mean molecular weight
- n_i: density of ith constituent
- N: total density ($N = \sum_i n_i$)
- ϕ_i: species flux ($\phi_i = n_i v_i$)
- T: temperature
- v_i: species diffusion velocity for ith species
- z: altitude

The turbulence was the initial physical process for the relationship described by equation (12) with the scale height and vertical gradient terms. Jones et al. (2017) used NCAR TGCMs to analyze the individual O transport components of O in the mesopause region including the advective component. They found the global annual mean advective velocity component to be ~ 20% of the eddy velocity component. Our assumption in this study is the advective component of vertical velocity is neglible. This will be considered in the discussion of errors, where the k_{zz} described here is an upper limit, and the actual values would be reduced by the same percentage.

2.3. Analysis and Results From the [O] Method

This 1-D approach is useful for long-term averaging. The analysis is confined to the middle and low latitudes, averaging for ~ 1 solar cycle.

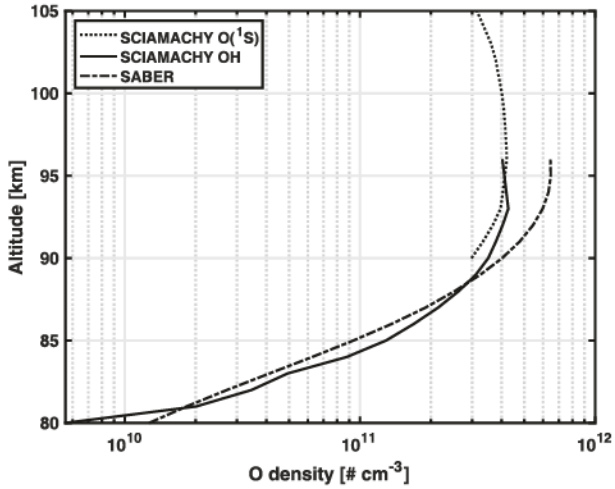

Figure 1. Global mean atomic oxygen density profiles from SCIAMACHY O(^{1}S) (dotted, Kaufmann et al., 2014), SCIAMACHY OH (solid, Zhu & Kaufmann, 2018), and SABER (dash dotted, Mlynczak et al., 2018) and S18).

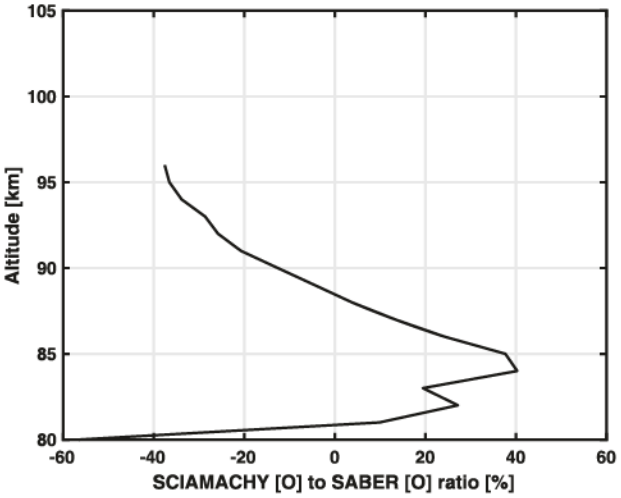

Figure 2. SCIAMACHY to SABER mean O density ratio in percent within the mesopause region. Positive percent means SCIAMACHY O is larger than SABER O.

The global mean SABER and SCIAMACHY O data used in this study are shown in Figure 1. The reader is referred to Zhu and Kaufmann (2018) for a comparison of SABER OH and SCIAMACHY OH data. Figure 2 describes the percent difference between the two, with larger O densities for SCIAMACHY between 82 and 88 km, and lower above and below. The large below 82 km may be due to the low quenching rates of OH($v = 8$) with O_2 used in the retrieval of SABER data by Mlynczak et al. (2018), which resulted in lower [O] derived from OH radiance measurements.

Figure 3 is a plot of the chemical loss rates for odd oxygen in the 80–105 km altitude region. The dominant loss process due to the HO_x chemistry (equation (5)), employed the global average climatology of SABER O_3 and H from Smith et al. (2013) and Mlynczak et al. (2018), respectively (large dashes). For comparison, the method of O_3 production (equation (5)) for SABER O (squares) and SCIAMACHY O (dash dot). Consequently, the downward flux of O is the same for both SABER and SCIAMACHY, but the respective O densities are responsible for differing eddy diffusion velocities, in this study. Note that the SABER O_3 production rate is equal to the ozone loss rate (dashed) since the SABER background atmosphere was calculated to force the two chemical rates to be equal (Mlynczak et al., 2018). Note the dominance of the loss of O via the three-body recombination rate, integrated between 80 and 105 km, is 2.6% that due to HO_x chemistry.

The loss rates of O described by the climatology of O_3 and H are used to calculate the eddy diffusion velocity (shown in Figure 4). The lower eddy diffusion velocity from SABER results from a larger [O] above 88 km. Below 88 km the eddy diffusion velocities of SABER and SCIAMACHY are approximately the same. For reference, the global and annual average total vertical transport velocity minus the molecular diffusion component calculated by Jones et al. (2017) from the National Center from Atmospheric Research (NCAR) thermosphere-ionosphere-mesosphere-electrodynamics general circulation model (TIME-GCM) is also shown in Figure 4. In section 3.3, we examine how the Jones et al. (2017) total vertical transport velocity of O compares to the eddy diffusion velocities calculated from SABER and SCIAMACHY.

The k_{zz} profiles deduced from SABER (solid) and SCIAMACHY (dashed) are depicted in Figure 5. The difference between the original k_{zz} shown from S18 (dotted) and the SABER k_{zz} derived herein (dashed) is ~ 20%, and is the result of using the global mean climatology of constituents (equation (5)) rather than the production rate of [O_3] (equation (4)) for the [O] loss rate, the background atmosphere, and the added temperature gradient term in equation (12). The differences in the SABER versus SCIAMACHY k_{zz} values are due to the respective O densities determining their eddy velocities and (1/[O]) × (d[O]/dz) term in equation (12).

3. Comparison of O Deduced k_{zz} With Other Results

3.1. Methodology and Results From [O_2]

[N_2] and [O_2] are the dominant well-mixed constituents of the background atmosphere through which the minor constituents diffuse in the upper mesosphere. The effect of recombination on the [O_2] distribution was determined by summing the total recombined O_2 for a night, which is 0.1%, or the maximum increase in the [O_2] at 88 km. The largest downward flux of [O] (and upward flux of [O_2]) is near the turbopause near 100 km. This was described by Colegrove et al. (1966) as a continuity condition for O and k_{zz} in that study. In this study, a calculation was made describing mass continuity of O, using global means of measured constituents from satellites.

A requirement of continuity for O and O_2 is the downward flux of O (lost in the mesosphere and O_2 production), which must be balanced by the upward flux of O_2 into the thermosphere, the source region of O. We chose to calculate the downward flux of O relative to the upward flux of O_2 to satisfy continuity at 100 km.

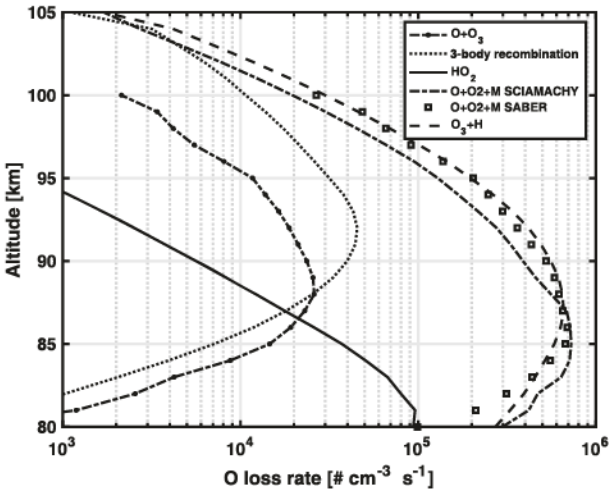

Figure 3. The chemical loss rates of odd oxygen versus altitude. The dominant loss is from the HO_x chemistry for both equation (4), that is, $O_3 + H$, and equation (5), $O + O_2 + M$. Equation (4) employed SABER O_3 by Smith et al. (2013) and of H by Mlynczak et al. (2018) (long dashes). A comparison is made O loss using equation (5) employing O from SABER (squares), and SCIAMACHY (dot-dash). Note the SABER results are identical (squares and dashes), but SCIAMACHY (dot-dash) differs slightly due to the different global mean O density profile. The minor losses from O three-body recombination (dots), $O + O_3$ (dot dash), and HO_2 chemistry (solid) have also been calculated with SABER climatologies of N_2 and O_2.

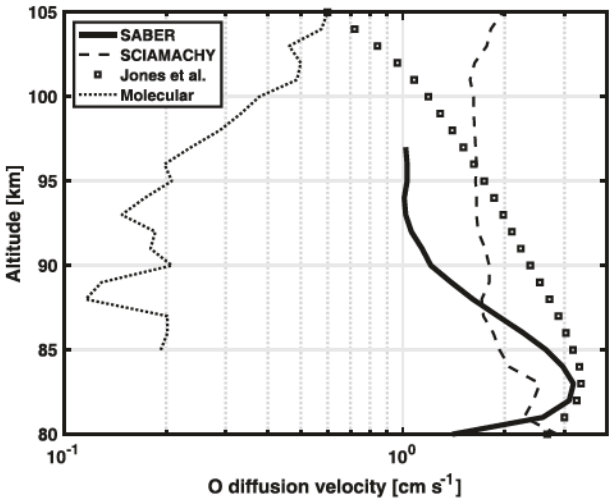

Figure 4. Atomic oxygen diffusive velocities versus altitude. Shown are the eddy diffusion profiles assuming SCIAMACHY (dashed) and SABER (solid) O densities and the total velocities from the flux deduced from the loss rates shown in equation (7). The eddy diffusion velocities are calculated from the total minus the molecular diffusion (small dots) and are directionally downward. The total velocity (less that by molecular diffusion) calculated by Jones et al. (2017) is plotted for comparison (squares).

For that, SCIAMACHY data extending up to 105 km and k_{zz} at 100 km were used in these calculations. The eddy and molecular transport velocities for O at 100 km are shown in Figure 4. Equation (10) was used to calculate the molecular diffusion velocity, and equation (13) (below) for the eddy velocity for O_2.

$$v_{O_2,eddy}(z=100) = -k_{zz}\left(\frac{1}{H + \frac{1}{T}\frac{dT}{dz} + \frac{1}{[O_2]}\frac{d[O_2]}{dz}}\right) \tag{13}$$

The total downward flux of atomic oxygen (8×10^{11} cm$^{-2}\cdot$ s^{-1}) results in a total, eddy, and molecular diffusion velocity values of 2.0, 1.6, and 0.4 cm/s, respectively. Note in Figure 4 the molecular diffusion velocity is 0.6 cm/s at 105 km and the eddy velocity for SCIAMACHY is ~ 3 times that value, whereas the diffusion coefficients are approximately equal (see Figure 6). This is largely explained by the dominance of the scale height term and difference between the molecular and eddy scale height values, which is nearly a factor of 2 for mass of O versus the mean molecular mass (see equation (10) and (12) for the effect). The required upward flux of O_2 from continuity is therefore 4×10^{11} cm$^{-2}\cdot$ s^{-1}. Using the SABER climatology deduced O_2 density, the total, eddy, and molecular diffusion velocities are 0.23, 0.15, and 0.07 cm/s, respectively. This calculated upward flux of O_2 is within ~10% of that determined from O. Consequently, the eddy diffusion coefficient determined from chemical loss of O also satisfies continuity requirement for the upward flux of O_2 near the turbopause.

In summary, the vertical flux of O and O_2 was determined for a critical altitude where O is chemically lost below and produced above. This satisfies continuity constraints with the calculated eddy and molecular diffusion, and SCIAMACHY determined k_{zz} at 100 km. The redistribution of the O_2 chemically produced in the MLT was considered. The total loss over a period of 10 days corresponds to a 1% change in O_2 density. Diffusion and advection processes are more than sufficient to redistribute the relatively small amount of chemically produced O_2 in the MLT.

3.2. Methodology and Results From [CO_2]

The CO_2 profiles are also from the SABER instrument. The CO_2 profiles only have daytime coverage. Detailed reasons behind the SABER CO_2 retrieval algorithm can be found in Rezac et al. (2015). For this work, all V2 SABER CO_2 profiles from February 2002 to December 2015 are utilized.

To calculate the global-mean CO_2 profiles, the SABER/TIMED CO_2 profiles were first binned evenly into 5° nonoverlapping latitude bins from 50°S to 50°N over a 2-month (yaw cycle) period with a 1-month overlap. Note here that this involved selecting the exact dates of the profiles and determining which month and year they belonged to. For example, the zonal-mean CO_2 profile for January 2003 comprises all profiles from 1 January 2003, to 28 February 2003, in order to account for the 60 day local time precession. Then, from these zonal-mean profiles, the cosine-of-latitude weighted global-mean CO_2 profiles were calculated. The observed global-mean profiles were then modeled using a one-dimensional photochemical and transport model (Allen et al., 1981; Liang et al., 2007; Salinas et al., 2016). However, the modeling approach in this paper is slightly different from the modeling approach of Salinas et al. (2016) to ensure that not only the apparent seasonal variations are captured, but also the other periodic and nonperiodic signals.

The SABER/TIMED profiles were first interpolated into the same pressure surfaces corresponding to 1-D model pressure surfaces. Then, the lower boundary CO_2 concentration of the model is matched with that observed. Finally, the model's k_{zz} profile is adjusted. The initial model profile is given by Allen et al. (1981). Specifically, the model's k_{zz} was adjusted at eight altitude bands: 72–75, 76–80, 82–85, 86–90, 92–95, 96–100, 102–105, and 106–110 km. Salinas et al. (2016) only modified the model's k_{zz} at three altitude bands.

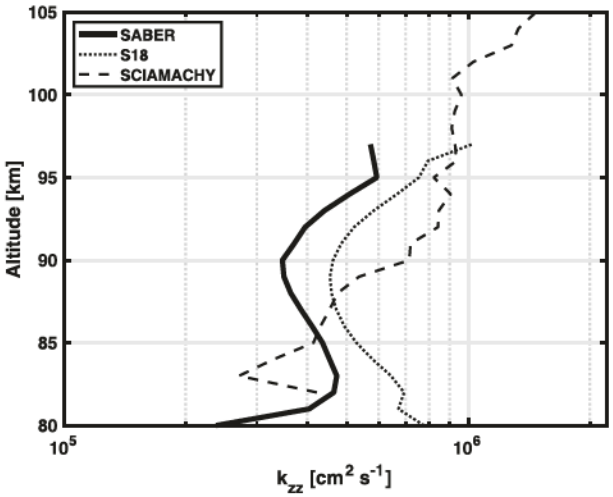

Figure 5. SCIAMACHY (dashed) and SABER (solid) k_{zz} values deduced from their respective O densities and using the eddy diffusion velocities shown in Figure 4. The SABER OH k_{zz} calculated here is ~ 20% less than the k_{zz} calculated by S18 (dotted).

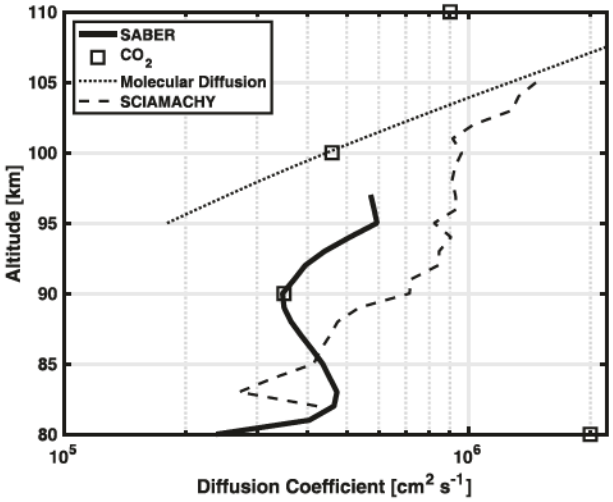

Figure 6. The eddy diffusion profiles from SCIAMACHY (dashed) and SABER (solid) are the same as Figure 5. The large squares are derived from SABER global CO_2 mean densities Salinas et al. (2016) and described in the text. The small dots are D_O, the molecular diffusion coefficient for O.

In modeling the profile, a simple iterative algorithm was used wherein each altitude band was multiplied by a scaling factor from bottom to the top. The initial factor is just 1 and is adjusted by increments of 0.1 until the root-mean-square (rms) is minimized. When the rms is minimized for a current altitude band, the algorithm then proceeds with the next altitude band above the current. The rms computed is between the modeled CO_2 and SABER CO_2. By "increments of 0.1"; this means that the adjustment factor is modified by either adding 0.1 or subtracting 0.1 depending on whether the rms is improved or not. After going through all altitude bands, adjustments are done again, beginning with the lowest altitude band. Two more rounds of adjustments are done with the 0.1 increment. Then, one round of adjustments is done with the increment reduced to 0.05 and finally, a last round of adjustments is done with the increment reduced to 0.01. Note that the choice of altitude bands, order of iteration, number of iterations and choice of increments are all arbitrary. As long as the rms is improved, the choices for these parameters does not matter. The k_{zz} profiles were determined from SABER CO_2 densities averaged between from February 2002 to December 2015.

The k_{zz} from CO_2, described above, is plotted in Figure 6. For historical perspective, there have been large differences between k_{zz} deduced from O versus CO_2 in the MLT region (e.g., Lopez-Puertas et al., 2000; Siskind et al., 2014 and S18). The k_{zz} calculated from OH emission (both SABER and SCIAMACHY) has a larger error below 85 km due to the distance below the centroid peak emission altitude of 88 km. SABER k_{zz}'s values for O and CO_2 compare well at 90 km. SABER k_{zz} from CO_2 are ~0.5 the values of SCIAMACHY at 100 km. All three profiles show increasing values above 90 km. This is the first time k_{zz} for CO_2 and O has been shown to be consistent between two different minor constituents measured by the same instruments, but processed differently, at least above 85 km. The k_{zz} calculated from CO_2 is much larger than from k_{zz} calculated from O at 80 km. The larger values of k_zz in CO_2 may be attributed to the weak vertical gradients around 80 km (Rezac et al., 2015). Weak vertical gradients generally mean that altering the mixing ratio distribution requires stronger vertical transport.

3.3. Comparison With Jones et al. (2017) Results

Jones et al. (2017) focused on understanding the relative contribution of MLT diffusion (eddy and molecular), dynamics, and chemistry to the globally averaged SAO in the upper thermosphere and ionosphere. They calculated the various global and annual average vertical transport velocities of O from a climatological NCAR's TIME-GCM simulation. Shown in Figure 4 (squares) is the "total" vertical transport velocity of O, consisting of the sum of the eddy, large-scale advective (i.e., by the mean vertical wind), and the net tidal (w' or vertical wind perturbation term; see Jones et al., 2017, for more details) transport velocities. These calculated velocities show that the eddy diffusion velocity component between 85 and 105 km (calculated from O using a similar equation to equation (9) above) accounts for ~50–60% of the total velocity shown in Figure 4. The general good agreement between the SABER, SCIAMACHY, and TIME-GCM supports the methodology used herein for calculating the global average k_{zz} values from a chemically reactive species, such as O.

4. Discussion and Uncertainties

The vertical diffusion velocity of atomic oxygen and k_{zz} computed in this study were determined from the climatologies of SABER and SCIAMACHY. The eddy diffusion velocity of O above 85 km is ~1–2 cm/s and slightly larger below 85 km. They were compared to the results of Jones et al. (2017), and showed favorable agreement.

k_{zz} is ~3–6 × 10^5 cm^2/s below 90 km, increasing above. SCIAMACHY k_{zz} increases from ~ 7 × 10^5 cm^2/s at 90 km to 0.9–1.2 × 10^6 cm^2/s at 105 km. The SCIAMACHY k_{zz} is increasing from a minimum near 80 km to a maximum above 100 km. k_{zz} was also calculated for SABER CO_2, which compared favorably with the calculation from SABER and SCIAMACHY O results, including their altitude.

The upward flux of O_2 was determined to be ~half of the downward flux of O at 100 km which is consistent with the continuity of O. The O_2 for that calculation and the background atmosphere for all the results presented in this study used a SABER-based climatology, from the same period as the SABER and SCIAMACHY O data.

This study deduced the total O velocity transport but could not differentiate components of turbulence, advection, gravity waves, tides, or tidal filtering of gravity waves as Jones et al. (2017). The issue with k_{zz} and the advection term is that it does not follow the relationship described in equation (11). Our assumptions have assumed that all components do, and consequently the k_{zz} determined here is an upper limit, with the true value reduced by the fraction of advection to the total. The fraction of the global average advective velocity by Figure 4 of Jones et al. (2017) to the SCIAMACHY total velocity is 0.15, 0.21, 0.32, and 0.35 at 100, 95, 90, and 85 km, respectively. The same fraction to the SABER total velocity is 0.35, 0.41, and 0.35 at 95, 90, and 85 km, respectfully. The formulation of the relationship between the effective O diffusion velocity and k_{zz} was originally derived for turbulent processes by Colegrove et al. (1965) and for gravity wave effects by Grygalashvyly et al. (2012) and Gardner (2018). The residual circulation with polar upwelling in summer and downwelling in the winter certainly is an advection process that primarily has a global effect on O at high latitudes. Gardner (2018) argues the advective contribution to vertical transport of O is minimal at middle and low latitudes, and larger in polar regions. Given that the global means in this study are equatorward of 55° latitude and the Jones et al. (2017) study included polar regions, the contributions described above may be an overestimate of a potential advective contribution to the long-term, global average vertical velocity of O in this study. A contribution from advection at high latitudes could be accomplished via the residual circulation where downwelling in the polar night transpires at a warmer temperature than in the upwelling region, where a temperature difference of an assumed 20 °C in the MLT results in a ~6% change in the integrated loss rate (see equation (4)). A planned study of intra-annual variations including latitudinal and seasonal effects in the vertical transport velocity will likely provide improved information on the advection contribution to the global mean determination of k_{zz} from O.

A brief discussion of diffusion processes and diffusive equilibrium is relevant. Mathematically, diffusive equilibrium is the condition that the flux divergence and eddy diffusive velocities are negligible. However, in the case of atomic oxygen, there is chemical production in the molecular diffusion regime and loss in the eddy diffusion regime. This requires a modeling of the diffusion coefficients and velocities in order to define the altitude distribution of minor constituents. Diffusion velocities are large (and diffusion times are short) in the thermosphere relative to the mesopause region. Lednyts'kyy et al. (2017) calculated a time delay of 13 days between the 27-day solar rotation cycle and the variation in O density at 90–100 km using SCIAMACHY data. The low diffusion velocities in the MLT (Figure 4), ranging 1.0–1.7 cm/s, translate to transport times of ~5 to 8 days between 88 km (the altitude of maximum O loss) and 95 km, the mean altitude used by Lednyts'kyy et al. (2017). Combining those times results in a total delay of 18–22 days for O to travel from 120 and 88 km. Delays between 120 km and the thermosphere would further add to these delays. These time delays are not normally an issue for model users since the density effect is the goal, and adjusting k_{zz} is a physically reasonable tool to accomplish that. We might ask "How does this compare to the chemical time to influence a significant change in the O density?" At 88 km, if replenishment ceases, the loss rate (i.e., $dn/dt = -L$) results in the O density e-folding in ~8 days. The bottom side O layer is very active chemically and diffusively. The high chemical loss rate shapes the O layer profile for the relatively slow O transport velocity (and k_{zz}) present.

The assumption herein is that diffusive transport of O from above 105 km is the source of all O in determination of the diffusion velocity and k_{zz} (i.e., there is no O production below that altitude). The uncertainty associated with this assumption is addressed below. The production of O in the mesosphere relative to the fraction produced in the thermosphere was addressed in S18 but is revisited considering the assumptions made in this study. Determination of dissociation rates in the mesosphere and thermosphere was performed by Solomon and Qian (2005). The total dissociation rate profile from 80–400 km shown in their Figure 5b

for the overhead Sun was integrated with altitude, with the resulting ratio of the production rate below versus above 105 km of ~2.8%. Their study ignored the predissociation of O_2 by the Schumann-Runge bands. That process was studied by Frederick and Hudson (1980), which is shown to be important below 92 km in their Figure 2. We calculated the predissociation production by applying the rates described in Table A2 of Frederick and Hudson (1980) and the O_2 densities determined herein (section 2.1). The integrated loss below 90 km contributes <0.3%, which combined with the EUV dissociation of ~2.8%, is ~3.1%. This fraction of O production by photodissociation and predissociation below and above 105 km is a relatively insignificant effect in the determination of k_{zz}.

Of note is the uncertainty in k_{zz}. Significant departures exist at 80 km between the k_{zz} determined from SABER and SCIAMACHY O densities and the k_{zz} determined from SABER CO_2. Above 82 km CO_2 is no longer well mixed and begins to exhibit a vertical gradient. We have no explanation for the significant increase of the k_{zz} from CO_2 below 85 km, or its divergence from k_{zz} determined from O. The uncertainty in O density increases significantly below 85 km, and marginal at best at 80 km, due to the weaker OH emission and noise induced by viewing through the layer from above.

The difference between O from SABER and that from SCIAMACHY, deduced from OH between 80 and 96 km, shown in Figure 2, is <20%. The relative uncertainty for a given platform (SABER and SCIAMACHY) is minuscule due to the large number of samples over the 11–16 years of measurements. We note the largest k_{zz} from SCIAMACHY global mean data is above 100 km. SCHIAMACHY measurements at these altitudes are made from the $O(^1S)$ emission, for which there is little uncertainty in the measurement interpretation. SCIAMACHY high-latitude data coverage extends 50–80°, whereas SABER data analyzed was equatorward of 55°. Note that SCIAMACHY $O(^1S)$ data above 65° in latitude was generally not used to derive atomic oxygen due to the effect of aurora, as shown in Figure 2 of Kaufmann et al. (2014). The high-latitude regions may have a bias in the advective component of velocity due to the residual circulation where there is upwelling in summer and downwelling in winter (Fritts & Alexander, 2003; Roble & Ridley, 1994). If there is a sampling bias for a given season or hemisphere, a bias may occur for the vertical component of the advective flux. The next phase of study is to compute seasonal and latitudinal profiles of O density for determinations of the transport velocities and k_{zz}. This may further elucidate the relative contributions of atomic oxygen in the MLT.

5. Summary and Conclusions

This study of global mean vertical transport of constituents (primarily O) in the MLT revised values of global averaged k_{zz} following the methodology of S18 but with notable improvements. Originally, S18 used [O] determined from SABER OH emission data (Mlynczak et al., 2018). Our reevaluated calculations in this study included the following:

(a) Determination of O loss in the mesosphere with $O_3 + H \rightarrow OH + O_2$, where the global mean densities were obtained directly from SABER O_3 by Smith et al. (2013) and H by Mlynczak et al. (2018).
(b) Global mean O densities are determined from SABER OH (same as S18, see Mlynczak et al., 2018) and from SCIAMACHY OH and $O(^1S)$ as described by Kaufmann et al. (2014) and Zhu and Kaufmann (2018).

The prominent results and conclusions to emerge from this study are the following:

(i) The eddy diffusion velocity of O above 85 km is ~1 to 1.7 cm/s and slightly larger below. A favorable comparison was found between the values determined in this study and that of Jones et al. (2017). This is important because k_{zz} is a powerful tuning parameter used in a number of general circulation models in the IT community to better produce observed mass, electron, and constituent densities. The time for an O atom to diffuse between 88 km altitude (where O is lost) and 120 km, where O is produced, is ~17 to 22 days.
(ii) The eddy diffusion coefficient (k_{zz}) calculated herein is ~3 to 6×10^5 cm^2/s below 90 km, increasing to ~0.9 to 1.2×10^6 cm^2/s at 105 km. The calculated values are a factor of 2 lower at 90 km where lidar studies suggest GWs are dominant, relative to the 100–105 km range. k_{zz} determined with SABER data in this study is ~20% lower than the values determined in S18.
(iii) k_{zz} was calculated for SABER CO_2 following Salinas et al. (2016) and compared favorably with SABER O k_{zz} above 85 km. The favorable comparison here differs from the history of large differences between k_{zz} derived from O versus CO_2.

The natural evolution to follow this is a study of the intra-annual variability in k_{zz} profiles in the MLT. The variability of k_{zz} for the SAO and the AO are largely unknown regarding the constituent climatologies in the MLT.

Acknowledgments
The support for F. Vargas and partial support for G. Swenson was provided by the NSFAGS17-59573 and NSF AGS 11-10334 grants. C.C.J.H. Salinas acknowledges support from Taiwan Ministry of Science and Technology Grants 107-2111-M-008-002-MY3, 108-2636-M-008-002, and 108-2811-M-008-505. The NCU Center for Astronautical Physics and Engineering is supported by The Higher Education Deep Cultivation program of the Taiwan Ministry of Education. A. Liu was partially supported by NSF Grant AGS-1115249. M. Jones, Jr., and D. P. Drob acknowledge support from NASA through the inter-agency agreement NNH17AE69I to the U.S. Naval Research Laboratory. The SABER data products presented in this paper are accessible from the SABER website (http://saber.gats-inc.com/data.php). J.H. Yee is partially supported by the NASATIMED Contract NNN06AA01C to the Johns Hopkins University, Applied Physics Laboratory. We thank ESA for providing the SCIAMACHY data within the Cat-1 project 2515. The SCIAMACHY Level 1b Version 8 data used in this study are available online (at ftp://scia-ftp-ds.eo.esa.int). We extend a special thank you to the two anonymous reviewers who made very constructive comments and suggestions to the manuscript.

References

Allen, M., Yung, Y. L., & Waters, J. W. (1981). Vertical transport and photochemistry in the terrestrial mesosphere and lower thermosphere (50 to 120 km). *Journal of Geophysical Research*, *86*(A5), 3617–3627.

Becker, E., & von Savigny, C. (2010). Dynamical heating of the polar summer mesopause induced by solar proton events. *Journal of Geophysical Research*, *115*, D00I18. https://doi.org/10.1029/2009JD012561

Catling, D. C., & Kasting, J. F. (2017). *Atmospheric evolution on inhabited and lifeless worlds*: Cambridge University Press. Online ISBN: 9781139020558, https://doi.org/10.1017/9781139020558

Catling, D. C., & Zahnle, K. J. (2009). Our planet's leaky atmosphere: As Earth's air slowly trickles away into space, will our planet come to look like Venus? Scientific American, May 1, 36–43.

Colegrove, F. D., Hanson, W. B., & Johnson, F. S. (1965). Eddy diffusion and oxygen transport in the lower thermosphere. *Journal of Geophysical Research*, *70*(19), 4931–4941.

Colegrove, F. D., Johnson, F. S., & Hanson, W. B. (1966). Atmospheric composition in the lower thermosphere. *Journal of Geophysical Research*, *71*(9), 2227–2236.

Fesen, C., & Hays, P. B. (1982). MG^+ morphology from Visual Airglow Experiment observations. *Journal of Geophysical Research*, *87*, 9217–9223.

Field, P. R., Rishbeth, H., Moffett, R. J., Wenden, D. W., Fuller-Rowell, T. J., Millward, G. H., & Aylward, A. D. (1998). Modelling composition changes in *F*-layer storms. *Journal of Atmospheric and Solar-Terrestrial Physics*, *60*(5), 523–543.

Frederick, J. E., & Hudson, R. D. (1980). Dissociation of molecular oxygen in the Schumann-Runge bands. *Journal of the Atmospheric Sciences*, *37*(5), 1099–1106.

Fritts, D. C., & Alexander, M. J. (2003). Gravity wave dynamics and effects in the middle atmosphere. *Reviews of Geophysics*, *41*(1), 1003. https://doi.org/10.1029/2001RG000106

Fritts, D. C., & Alexander, M. J. (2012). Correction to "Gravity wave dynamics and effects in the middle atmosphere. *Reviews of Geophysics*, *50*, RG3004. https://doi.org/10.1029/2012RG000409

Fukao, S., Yamanaka, M. D., Ao, N., Hocking, W. K., Sato, T., Yamamoto, M., & Kato, S. (1994). Seasonal variability of vertical eddy diffusivity in the middle atmosphere: 1. Three-year observations by the middle and upper atmosphere radar. *Journal of Geophysical Research*, *99*(D9), 18,973–18,987.

Fuller-Rowell, T. J. (1998). The 'Thermospheric Spoon': A mechanism for the semiannual density variation. *Journal of Geophysical Research*, *103*(A3), 3951–3956.

Garcia, R. R., López-Puertas, M., Funke, B., Marsh, D. R., Kinnison, D. E., Smith, A. K., & González-Galindo, F. (2014). On the distribution of CO_2 and CO in the mesosphere and lower thermosphere. *Journal of Geophysical Research: Atmospheres*, *119*, 5700–5718. https://doi.org/10.1002/2013JD021208

Gardner, C. S. (2018). Role of wave-induced diffusion and energy flux in the vertical transport of atmospheric constituents in the mesopause region. *Journal of Geophysical Research: Atmospheres*, *123*, 6581–6604. https://doi.org/10.1029/2018JD028359

Gardner, J. A., Broadfoot, A. L., McNeil, W. J., Lai, S. G., & Murad, E. (1999). Analysis and modeling of the GLO-1 observations of meteoric metals in the thermosphere. *Journal of Atmsopheric and Solar-Terrestrial Physics*, *61*(7), 545–562.

Gardner, C. S., & Huang, W. (2016). Impact of horizontal transport, temperature, and PMC uptake on mesospheric Fe at high latitudes. *Journal of Geophysical Research: Atmospheres*, *121*, 6564–6580. https://doi.org/10.1002/2015JD024674

Gardner, C. S., & Liu, A. Z. (2010). Wave-induced transport of atmospheric constituents and its effect on the mesospheric Na layer. *Journal of Geophysical Research*, *115*, D20302. https://doi.org/10.1029/2010JD014140

Gardner, C. S., & Liu, A. Z. (2014). Measuring eddy heat, constituent, and momentum fluxes with high-resolution Na and Fe Doppler lidars. *Journal of Geophysical Research: Atmospheres*, *119*, 10,583–10,603. https://doi.org/10.1002/2013JD021074

Gardner, C. S., Liu, A. Z., Marsh, D. R., Feng, W., & Plane, J. M. C. (2014). Inferring the global cosmic dust influx to the Earth's atmosphere from lidar observations of the vertical flux of mesospheric Na. *Journal of Geophysical Research: Space Physics*, *119*, 7870–7879. https://doi.org/10.1002/2014JA020383

Gerard, J. C., & Monfils, A. (1978). MG^+ equatorial airglow altitude distribution. *Journal of Geophysical Research*, *83*, 4389–4391.

Grygalashvyly, M., Becker, E., & Sonnemann, G. R. (2011). Wave mixing effects on minor chemical constituents in the MLT region: Results from a global CTM driven by high-resolution dynamics. *Journal of Geophysical Research*, *116*, D18302. https://doi.org/10.1029/2010JD015518

Grygalashvyly, M., Becker, E., & Sonnemann, G. R. (2012). Gravity wave mixing and effective diffusivity for minor chemical constituents in the mesosphere/lower thermosphere. *Space Science Reviews*, *168*(1), 333–362.

Guo, Y., Liu, A. Z., & Gardner, C. S. (2017). First Na lidar measurements of turbulence heat flux, thermal diffusivity, and energy dissipation rate in the mesopause region. *Geophysical Research Letters*, *44*, 5782–5790. https://doi.org/10.1002/2017GL073807

Hunten, D. M. (1973). The escape of light gases from planetary atmospheres. *Journal of the Atmospheric Sciences*, *30*(8), 1481–1494.

Hunten, D. M., & Strobel, D. F. (1974). Production and escape of terrestrial hydrogen. *Journal of the Atmospheric Sciences*, *31*(2), 305–317.

Jacchia, L. G. (1964). Static diffusion models of the upper atmosphere with empirical temperature profiles. SAO Special Report, 170.

Jacchia, L. G. (1970). New static models of the thermosphere and exosphere with empirical temperature profiles. SAO Special Report, 313.

Jacchia, L. G. (1971). Semiannual variation in the heterosphere: A reappraisal. *Journal of Geophysical Research*, *76*(19), 4602–4607.

Jeans, J. (2009). *The dynamical theory of gases* (4th ed.)., Cambridge Library Collection—Physical Sciences. Cambridge: Cambridge University Press.

Jones, M., Emmert, J. T., Drob, D. P., Picone, J. M., & Meier, R. R. (2018). Origins of the thermosphere-ionosphere semiannual oscillation: Reformulating the 'Thermospheric Spoon' mechanism. *Journal of Geophysical Research: Space Physics*, *123*, 931–954. https://doi.org/10.1002/2017JA024861

Jones, M., Emmert, J. T., Drob, D. P., & Siskind, D. E. (2017). Middle atmosphere dynamical sources of the semiannual oscillation in the thermosphere and ionosphere. *Geophysical Research Letters*, *44*, 12–21. https://doi.org/10.1002/2016GL071741

Jones, M., Forbes, J. M., & Hagan, M. E. (2014). Tidal-induced net transport effects on the oxygen distribution in the thermosphere. *Geophysical Research Letters*, *41*, 5272–5279. https://doi.org/10.1002/2014GL060698

Kaufmann, M., Zhu, Y., Ern, M., & Riese, M. (2014). Global distribution of atomic oxygen in the mesopause region as derived from SCIAMACHY O(^{1}S) green line measurements. *Geophysical Research Letters*, *41*, 6274–6280. https://doi.org/10.1002/2014GL060574

Khattatov, B. V., Geller, M. A., Yubin, V. A., & Hays, P. B. (1996). Diurnal migrating tide as seen by the high-resolution Doppler imager/UARS: 2. Monthly mean global zonal and vertical velocities, pressure, temperature, and inferred dissipation. *Journal of Geophysical Research*, *102*(D4), 4423–4435.

Kirchhoff, V. W. J. H., & Clemesha, B. R. (1983). Eddy diffusion coefficients in the lower thermosphere. *Journal of Geophysical Research*, *88*(A7), 5765–5768.

Lal, C. (1992). Global F_2 layer ionization and geomagnetic activity. *Journal of Geophysical Research*, *97*(A8), 12,153–12,159.

Lal, C. (1998). Solar wind and equinoctial maxima in geophysical phenomena. *Journal of Atmospheric and Solar-Terrestrial Physics*, *60*(10), 1017–1024.

Lednyts'kyy, O., von Savigny, C., & Weber, M. (2017). Sensitivity of equatorial atomic oxygen in the MLT region to the 11-year and 27-day solar cycles. *Journal of Atmospheric and Solar-Terrestrial Physics*, *162*, 136–150. Layered Phenomena in the Mesopause Region.

Liang, M.-C., Blake, G., Lewis, B., & Yung, Y. (2007). Oxygen isotopic composition of carbon dioxide in the middle atmosphere. *PNAS; Proceedings of the National Academy of Sciences*, *104*(1), 21–25.

Liu, A. Z. (2009). Estimate eddy diffusion coefficients from gravity wave vertical momentum and heat fluxes. *Geophysical Research Letters*, *36*, L08806. https:/doi.org/10.1029/2009GL037495

Liu, H.-L., Bardeen, C. G., Foster, B. T., Lauritzen, P., Liu, J., Lu, G., & Wang, W. (2018). Development and validation of the whole atmosphere community climate model with thermosphere and ionosphere extension (WACCM-X 2.0). *Journal of Advances in Modeling Earth Systems*, *10*, 381–402. https:/doi.org/10.1002/2017MS001232

Liu, S. C., & Donahue, T. M. (1974). Mesospheric hydrogen related to exospheric escape mechanisms. *Journal of the Atmospheric Sciences*, *31*(5), 1466–1470.

Liu, A. Z., & Gardner, C. S. (2005). Vertical heat and constituent transport in the mesopause region by dissipating gravity waves at Maui, Hawaii (20.7° N), and Starfire Optical Range, New Mexico (35° N). *Journal of Geophysical Research*, *110*, D09S13. https://doi.org/10.1029/2004JD004965

Liu, A. Z., Guo, Y. F., Vargas, F., & Swenson, G. R. (2016). First measurement of horizontal wind and temperature in the lower thermosphere (105–140 km) with Na lidar at Andes Lidar Observatory. *Geophysical Research Letters*, *43*, 2374–2380. https://doi.org/10.1002/2016GL068461

Lopez-Puertas, M., Garcia, M. A., & Roble, R. G. (2000). A review of CO_2 and CO abundances in the middle atmosphere, In Atmospheric science across the stratopause. *American Geophysical Union Geophysical Monograph Series*, *123*, 83–100.

Lübken, F.-J. (1997). Seasonal variation of turbulent energy dissipation rates at high latitudes as determined by in-situ measurements of neutral density fluctuations. *Journal of Geophysical Research*, *102*(D12), 13,441–13,456.

Mende, S. B., Swenson, G. R., & Miller, K. L. (1985). Observations of *E*-region MG^+ from SPACELAB-1. *Journal of Geophysical Research*, *90*, 6667–6673.

Mlynczak, M. G., Hunt, L. A., Marshall, B. T., Mertens, C. J., Marsh, D. R., Smith, A. K., et al. (2014). Atomic hydrogen in the mesopause region derived from SABER: Algorithm theoretical basis, measurement uncertainty, and results. *Journal of Geophysical Research: Atmospheres*, *119*, 3516–3526. https://doi.org/10.1002/2013JD021263

Mlynczak, M. G., Hunt, L. A., Mast, J. C., Thomas Marshall, B., Russell, J. M., Smith, A. K., et al. (2013). Atomic oxygen in the mesosphere and lower thermosphere derived from SABER: Algorithm theoretical basis and measurement uncertainty. *Journal of Geophysical Research: Atmospheres*, *118*, 5724–5735. https://doi.org/10.1002/jgrd.50401

Mlynczak, M. G., Hunt, L. A., Russell, J. M., & Marshall, B. T. (2018). Updated SABER night atomic oxygen and implications for SABER ozone and atomic hydrogen. *Geophysical Research Letters*, *45*, 5735–5741. https://doi.org/10.1029/2018GL077377

Paetzold, H. K., & Zschörner, H. (1961). An annual and a semiannual variation of the upper air density. *Geofisica pura e applicata*, *48*(1), 85–92.

Pilinski, M. D., & Crowley, G. (2015). Seasonal variability in global eddy diffusion and the effect on neutral density. *Journal of Geophysical Research: Space Physics*, *120*, 3097–3117. https://doi.org/10.1002/2015JA021084

Plane, J. M. C., Feng, W., & Dawkins, E. C. M. (2015). The mesosphere and metals: Chemistry and changes. *Chemical Reviews*, *115*(10), 4497–4541. PMID: 25751779.

Prolss, G. W. (1995). Ionospheric F region storms In *Handbook of Atmospheric Electrodynamics*, edited by H. Volland (pp. 195248). Boca Raton: CRC Press.

Qian, L., Burns, A. G., Solomon, S. C., & Wang, W. (2013). Annual/semiannual variation of the ionosphere. *Geophysical Research Letters*, *40*, 1928–1933. https://doi.org/10.1002/grl.50448

Qian, L., Solomon, S. C., & Kane, T. J. (2009). Seasonal variation of thermospheric density and composition. *Journal of Geophysical Research*, *114*, A01312. https://doi.org/10.1029/2008JA013643

Rao, D. N., Ratnam, M. V., Rao, T. N., & Rao, S. V. B. (2001). Seasonal variation of vertical eddy diffusivity in the troposphere, lower stratosphere and mesosphere over a tropical station. *Annales Geophysicae*, *19*, 975–984. https:/doi.org/10.5194/angeo-19-975-2001

Rezac, L., Jian, Y., Yue, J., Russell, J. M., Kutepov, A., Garcia, R., et al. (2015). Validation of the global distribution of CO_2 volume mixing ratio in the mesosphere and lower thermosphere from SABER. *Journal of Geophysical Research: Atmospheres*, *120*, 12,067–12,081. https://doi.org/10.1002/2015JD023955

Roble, R. G., & Ridley, E. C. (1994). A thermosphere-ionosphere-mesosphere-electrodynamics general circulation model (TIME-GCM): Equinox solar cycle minimum simulations (30–500 km). *Geophysical Research Letters*, *21*(6).

Russell, J. M., Mlynczak, M. G., Gordley, L. L., Tansock, J. J., & Esplin, R. W. (1999). Overview of the SABER experiment and preliminary calibration results. Proc. SPIE 3756, Optical Spectroscopic Techniques and Instrumentation for Atmospheric and Space Research III.

Salinas, C. C. J. H., Chang, L. C., Liang, M.-C., Yue, J., Russell, J., & Mlynczak, M. (2016). Impacts of SABER CO_2-based eddy diffusion coefficients in the lower thermosphere on the ionosphere/thermosphere. *Journal of Geophysical Research: Space Physics*, *121*, 12,080–12,092. https://doi.org/10.1002/2016JA023161

Sander, S. P., Golden, D. M., Kurylo, M. J., Moortgat, G. K., Wine, P. H., Ravishankara, A. R., et al. (2011). Chemical kinetics and photochemical data for use in atmospheric studies evaluation number 15. JPL Publication, 10, 6.

Sasi, M., & Vijayan, L. (2001). Turbulence characteristics in the tropical mesosphere as obtained by MST radar at Gadanki (13.5 N, 79.2 E). *Annales Geophysicae*, *19*, 1019–1025. https:/doi.org/10.5194/angeo-19-1019-2001

Sheese, P. E., McDade, I. C., Gattinger, R. L., & Llewellyn, E. J. (2011). Atomic oxygen densities retrieved from Optical Spectrograph and Infrared Imaging System observations of O_2A-band airglow emission in the mesosphere and lower thermosphere. *Journal of Geophysical Research*, *116*. https://doi.org/10.1029/96RG02213

Shizgal, B. D., & Arkos, G. G. (1996). Nonthermal escape of the atmospheres of Venus, Earth, and Mars. *Reviews of Geophysics*, *34*(4), 483–505.

Siskind, D. E., Drob, D. R., Dymond, K. E., & McCormac, J. P. (2014). Simulations of the effects of vertical transport on the thermosphere and ionosphere using two coupled models. *Journal of Geophysical Research: Space Physics*, *119*, 1172–1185. https://doi.org/10.1002/2013JA019116

Smith, A. K., Garcia, R. R., Marsh, D. R., & Richter, J. H. (2011). WACCM simulations of the mean circulation and trace species transport in the winter mesosphere. *Journal of Geophysical Research*, *116*. https://doi.org/10.1029/2011JD016083

Smith, A. K., Harvey, V. L., Mlynczak, M. G., Funke, B., García-Comas, M., Hervig, M., et al. (2013). Satellite observations of ozone in the upper mesosphere. *Journal of Geophysical Research: Atmospheres*, *118*, 5803–5821. https://doi.org/10.1002/jgrd.50445

Smith, A. K., Marsh, D. R., Mlynczak, M. G., & Mast, J. C. (2010). Temporal variations of atomic oxygen in the upper mesosphere from SABER. *Journal of Geophysical Research*, *115*. https://doi.org/10.1029/2009JD013434

Solomon, S. C., & Qian, L. (2005). Solar extreme-ultraviolet irradiance for general circulation models. *Journal of Geophysical Research*, *110*. https://doi.org/10.1029/2005JA011160

Swenson, G., Yee, Y., Vargas, F., & Liu, A. (2018). Vertical diffusion transport of atomic oxygen in the mesopause region consistent with chemical losses and continuity: Global mean and inter-annual variability. *Journal of Atmospheric and Solar-Terrestrial Physics*, *178*, 47–57.

Walterscheid, R. L. (1982). The semiannual oscillation in the thermosphere as a conduction mode. *Journal of Geophysical Research*, *87*(A12), 10,527–10,535.

Zhu, Y., & Kaufmann, M. (2018). Atomic oxygen abundance retrieved from SCIAMACHY hydroxyl nightglow measurements. *Geophysical Research Letters*, *45*, 9314–9322. https://doi.org/10.1029/2018GL079259